

Kinetics and Structural Investigation of Layered $\text{Li}_9\text{V}_3(\text{P}_2\text{O}_7)_3(\text{PO}_4)_2$ as a Cathode Material for Li-Ion Batteries

Prasanth Balasubramanian,^[a] Marilena Mancini,^{*,[a]} Holger Geßwein,^[b] Dorin Geiger,^[c] Peter Axmann,^[a] Ute Kaiser,^[c] and Margret Wohlfahrt-Mehrens^[a]

Cathode materials with improved safety and energy densities are required for developing next-generation Li-ion battery technology. Among different phosphate-based materials, layered $\text{Li}_9\text{V}_3(\text{P}_2\text{O}_7)_3(\text{PO}_4)_2$ (LVPP) has recently been explored as a high-voltage cathode. We report the feasibility of multi-electron reactions and the influence of crystallite size on the electrode kinetics. The mechanism of Li extraction/insertion during charge and discharge is investigated and the structural transformations

at high voltages are studied by means of in situ and ex situ analysis. The changes induced by electrochemical Li extraction are found to be reversible during cycling in the potential window of 2–4.6 V, whilst voltage profile changes and capacity fading is observed by charging up to 4.8 V, owing to irreversible phase transition and reduction of the interlayer distance. The findings can be applied for optimizing material synthesis as well as the working conditions in Li-ion battery applications.

1. Introduction

After the development and commercialization of olivine LiFePO_4 (LFP), other Li metal phosphates have gained considerable attention as potential cathode materials for Li-ion battery applications.^[1,2] This is because transition metal phosphates such as LiMPO_4 ($\text{M} = \text{Ni}, \text{Co}, \text{Mn}$) can reach specific energy values comparable to standard oxides, operate at higher voltages while concurrently being less expensive.^[2,3] Moreover, the strong covalent bond between phosphorus and oxygen is expected to provide increased chemical and thermal stability which makes phosphates suitable candidates to design high voltage and high capacity cathode materials for Li-ion batteries.^[3,4] Despite these advantages, structural degradation and electrolyte instability affect the electrochemical behavior of high voltage phosphate-based cathodes such as LiCoPO_4 and LiNiPO_4 and thus limiting their practical applications.^[5,6] Structural degradation of cathode active materials can occur during cycling due to different reasons such as the instability of the de-lithiated phase, structural defects and changes of the unit

cell volume during Li extraction/insertion with consequent conductivity loss due to cracking, etc.^[7] On the other hand, the electrochemical instability of most common liquid electrolyte systems is also a very critical issue at potentials of operation higher than 4.5 V.^[8] It is well-known that the instability of the electrolyte at high potentials can trigger degradation reactions between solvents such as propylene carbonate (PC), ethylene carbonate (EC) and di-methyl carbonate (DMC), ethyl methyl carbonate (EMC) and active cathode materials. Additional concern is the reactivity of LiPF_6 with trace amounts of H_2O to form HF, which then acts as corrosive agent causing structural degradation.^[9,10] All these phenomena taking place upon high potentials or during deep de-lithiation of cathode structure can cause severe capacity fading and voltage drop which limit the cell cycle life.^[9,11]

Vanadium-based phosphates have been gaining considerable attention as alternative cathode materials because they can exchange more than one electron per transition metal at potentials higher than LiFePO_4 and lower than LiCoPO_4 or LiNiPO_4 . For example, studies on $\text{Li}_3\text{V}_2(\text{PO}_4)_3$, polymorphs of LiVOPO_4 , Li_2VOPO_4 , LiVP_2O_7 , and on the analogous sodium compounds have been recently reported in literature.^[12,13,14] Among the different members of the high voltage phosphates, $\text{Li}_3\text{V}_2(\text{PO}_4)_3$ (LVP) stands out having an average working potential of 4.1 V. LVP shows high theoretical capacity of 197 mAh g^{-1} when three Li ions per formula unit are extracted/inserted.^[12] From a practical point of view, however, only two Li ions can be reversibly cycled without capacity fading and thus a maximum specific capacity 131 mAh g^{-1} is practically achieved. Cycling to very high potentials such as 4.8 V leads to rapid capacity fading as well as a voltage drop.^[14,15] Various explanations have been reported for this behavior, such as the dissolution of vanadium, electronic conductivity change during Li extraction, modifications in the vanadium environment at complete de-lithiation and reactivity of the electrolyte with the unstable de-lithiated structure.^[10,14,15,16] Such fundamental

[a] P. Balasubramanian, Dr. M. Mancini, Dr. P. Axmann, Dr. M. Wohlfahrt-Mehrens

Accumulators Material Research
Zentrum für Sonnenenergie und Wasserstoff-Forschung
Baden-Württemberg (ZSW)
Helmholtzstraße 8, 89081 Ulm, Germany
E-mail: marilena.mancini@zsw-bw.de

[b] Dr. H. Geßwein

Institut für Angewandte Materialien und
Keramische Werkstoffe und Technologien (IAM-KWT)
Karlsruher Institut für Technologie (KIT)
Hermann-von-Helmholtz-Platz 1, Gebäude 575
76344 Eggenstein-Leopoldshafen, Germany

[c] Dr. D. Geiger, Prof. Dr. U. Kaiser

Materialwissenschaftliche Elektronenmikroskopie
Universität Ulm
Albert-Einstein-Allee 11, 89081 Ulm, Germany



Supporting information for this article is available on the WWW under
<https://doi.org/10.1002/celc.201700734>

understanding of the cathode material behavior and its failure mechanisms can be helpful to improve the electrochemical performance and explore its feasibility for practical applications. Recently, another vanadium-based Li monodiphosphate $\text{Li}_9\text{V}_3(\text{P}_2\text{O}_7)_3(\text{PO}_4)_2$ (LVPP) has been explored as high voltage cathode material for Li-ion batteries.^[17] Detailed DFT-based theoretical studies on LVPP, have been carried out by Ceder and his coworkers.^[18] Similar to LVP, LVPP can also be cycled within different potential windows, such as 2–4.6 and 2–4.8 V. We recently reported that controlling the growth of crystallites during synthesis can effectively improve cycling stability and rate capability of LVPP.^[19] However, open questions on the transport properties within the lattice, changes in the structure and phase transformation during delithiation / lithiation, need to be addressed in order to further improve the electrochemical performance of LVPP.

In the present study, the electrochemical behavior of micro-crystalline and nano-crystalline LVPP is studied using electrochemical techniques such as cyclic voltammetry (CV), galvanostatic charge/discharge cycles and electrochemical impedance spectroscopy (EIS). The pristine structure is fully resolved by high resolution transmission electron microscopy (HR-TEM). Furthermore, in situ and ex situ X-ray diffraction (XRD) and Fourier transformed Infra-red spectroscopy (FTIR) were used to track the structural changes during cycling. The changes in the crystal lattice of LVPP induced by Li extraction/insertion and their correlation with the operating potential window are reported.

2. Results and Discussion

2.1. Structural and Morphological Characterization

The synthesized micro-crystalline (M-LVPP) and nano-crystalline (N-LVPP) LVPP samples were analyzed using XRD to check the phase purity of the crystalline phases. The XRD patterns of the two samples are reported in Figure 1a and b.

All diffraction peaks were identified and indexed based on the $\text{Li}_9\text{Fe}_3(\text{P}_2\text{O}_7)_3(\text{PO}_4)_2$ (PDF#49-0207), that belongs to the $P-3c1$

space group. Both samples show phase-pure LVPP and no additional crystalline phases are identified. Furthermore, the Rietveld refinement of the measured patterns was carried out and the lattice parameters are given in Table 1. The goodness

Table 1. Lattice parameters and crystallite size of LVPP samples from XRD analysis.

Sample name	a [Å]	c [Å]	Volume [Å ³]	Crystallite size [nm]	χ^2
M-LVPP	9.740 (41)	13.622 (78)	1119.70 (14)	190	1.16
N-LVPP	9.742 (15)	13.631 (37)	1122.23 (05)	40	1.22

of fit χ^2 is close to 1 for both the samples, indicating a good reliability of the results. The diffraction pattern of sample M-LVPP in Figure 1a shows very sharp peaks, as expected due to the micro-crystalline nature of LVPP. The crystallite size of M-LVPP was calculated as 190 nm. On the other hand, the diffraction pattern of sample N-LVPP shows much broader peaks, which is characteristic of powders with nano-sized crystallites. The mean crystallite size was calculated as 43 nm for N-LVPP. The morphology of the samples was examined by SEM. Figures 1c and d display the in-lens images of samples M-LVPP and N-LVPP, respectively. Due to the ball milling treatment, sample N-LVPP presents smaller particles, while sample M-LVPP shows larger particles. Chemical analysis reveals a carbon content of 4.4 wt.% for both samples.

In order to confirm the phase purity and the structure, HR-TEM investigation was carried out. The material is highly electron-beam-sensitive leading to fast amorphization of the structure during exposure in TEM, which made the zone axis orientation and the consecutive thickness characterization by using TEM image simulations more difficult (Figure 1 Supplement information). Therefore, the imaging was carried out not only at 300 kV but also at 80 kV, where limited knock-on damage is induced by the beam energy, however both allowing atomic resolution. As shown in Figure 2a, the diffraction patterns of the LVPP particles shows mostly isotropic distributed Bragg reflections. This confirms the polycrystalline nature of the synthesized LVPP material. Figure 2b indicates that the synthesized LVPP exhibits a layered structure. Figure 2c shows occasionally overlapped thin layers of LVPP, which are rotated towards each other as seen by the Moiré pattern formed. Unambiguous identification of the LVPP crystal structure has been achieved by measuring crystal plane distances at different orientations and comparing TEM images with corresponding simulations. Figure 2d shows crystal planes in atomic resolution at 300 kV. The crystal plane distance, calculated as 0.843 nm, corresponds to the $(10\bar{1}0)$ plane of the hexagonal unit cell, in good agreement with what has been reported in literature.^[17] Figure 2e shows the $[0001]$ -oriented LVPP crystal grain imaged at 300 kV. The white framed sub-image is enlarged on the right and is partially overlapped with the corresponding simulation (red border). The estimated thickness of 12 unit cells = 16.3 nm resulted from the best fit between simulated and experimental

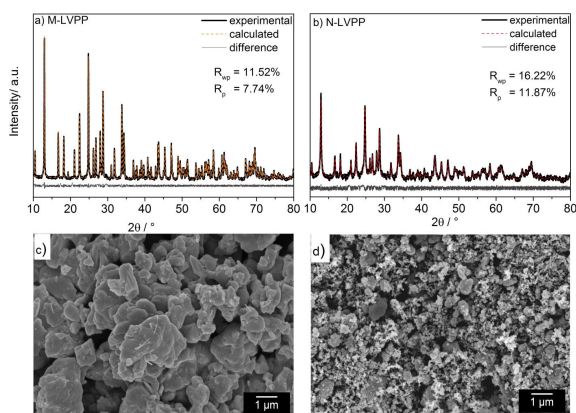


Figure 1. X-Ray diffraction patterns of a) M-LVPP and b) N-LVPP. SEM images of c) M-LVPP and d) N-LVPP.

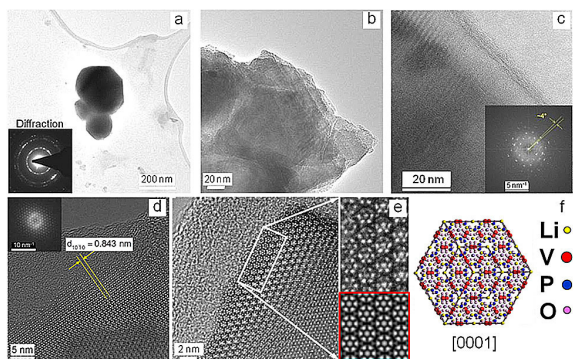


Figure 2. a) Image and diffraction pattern of LVPP particles. b) Typical layer-wise-structured polycrystalline powder particle. c) HR-TEM image taken at 80 kV with diffraction pattern showing parallel Moiré fringes. d) (1010) Crystal planes in atomic resolution at 300 kV. e) [0001]-Oriented LVPP crystal grain with sub-image, which is partially overlapped with simulation (red frame) corresponding to a 12 unit cell thickness. f) Projected crystal structure of LVPP in [0001] orientation.

image. Figure 2f displays the projected crystal structure of LVPP in [0001] orientation for better understanding. Similar results were obtained from HR-TEM images acquired at 80 kV accelerating voltage confirming the structure of LVPP. The structural analysis made by HR-TEM agrees with the XRD results reported above and shows that the synthesized LVPP is phase-pure and has a layered structure with hexagonal unit cell.

2.2. Electrochemical Investigation

The galvanostatic charge/discharge profiles of M-LVPP and N-LVPP at room temperature have been already reported in our previous paper.^[19] Improved discharge capacity and high rate capability were obtained for electrodes based on N-LVPP. In order to gain insight into the kinetics of the Li ion extraction/insertion process in the layered $\text{Li}_9\text{V}_3(\text{P}_2\text{O}_7)_3(\text{PO}_4)_2$ structure, cyclic voltammograms at different scan rates were recorded in the present study. Cyclic voltammetry (CV) represents a very useful electrochemical technique which is often used for determining the reversibility of electrochemical processes. It is also possible to use CV to calculate the average diffusion coefficient of Li by applying the Randles-Sevcik equation $i_p = 2.69 \times 10^5 n^{3/2} A D^{1/2} \nu^{1/2} C_0$.^[20,21] In this equation, i_p is the peak current (A), n the number of electrons transferred per molecule of oxidized or reduced species, A the area of the electrode (cm^2), ν the voltage scan rate (Vs^{-1}), C_0 the concentration of oxidized or reduced species in solution (mol cm^{-3}) and D the chemical diffusion coefficient ($\text{cm}^2 \text{s}^{-1}$). In the case of Li ion diffusion into a solid composite electrode such as a cathode for Li-ion batteries, the measured value is termed as 'apparent' diffusion coefficient as it is assumed to be constant over the measured potential of which is theoretically not possible and we assume that the redox process is fully reversible.^[21] Despite the limitations of the defined parameters, CV analysis is often applied to anode and cathode materials for Li-ion batteries to evaluate, for example, the dependence of the electrode kinetics on the size of the active material.^[20] In an attempt to study the

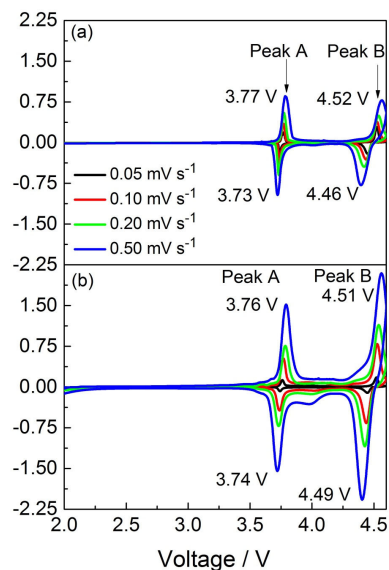


Figure 3. Cyclic voltammograms at different scan rates for electrodes based on a) M-LVPP and b) N-LVPP.

kinetics of LVPP-based cathodes and the influence of crystallite size, CV analysis has been performed at different scan rates, namely 0.05, 0.1, 0.2 and 0.5 mVs^{-1} . In Figure 3a and 3b, we report the cyclic voltammograms of electrodes made with M-LVPP and N-LVPP, respectively.

For both samples, we can clearly identify two main electrochemical processes within the investigated potential range. At a scan rate of 0.05 mVs^{-1} , the first electrochemical process corresponding to the current peak A occurs at 3.77 V and 3.73 V during oxidation and reduction, respectively. A second current peak, B, occurs at higher voltages, namely at 4.52 V and 4.46 V during oxidation and reduction, respectively. As expected, with increasing scan rate the anodic peak potential shifts to higher voltages and the cathodic peak potential shifts to lower voltages. At the same time, the current peaks become broader with increasing scan rate. This is due to the increased polarization at higher sweep rates because of kinetic limitations associated with the Li ion diffusion through the active material. In the applied potential window, the voltammograms of N-LVPP electrodes show higher current peaks than those of M-LVPP, indicating faster kinetics of the Li extraction/insertion processes. For both low and high voltage processes, the analysis of the voltammograms shows that the voltage separation between anodic and cathodic current peak, i.e. $\Delta E = E_{pa} - E_{pc}$, is much smaller in the case of nano-sized crystals, (N-LVPP). At 0.05 mVs^{-1} scan rate, the ΔE of the peaks A and B is respectively 20 mV and 40 mV smaller for N-LVPP than for M-LVPP (see values in Figure 3).

Figures 4a and 4b show the plot of the measured redox peak currents (i_p) vs. the square root of the scan rate ($\nu^{1/2}$) for N-LVPP and M-LVPP electrodes for process A and B, respectively. The plots have a linear behavior, which is expected for the diffusion-limited Li insertion/extraction processes. The slope of the plots, which corresponds to the diffusion coefficient, is strongly dependent on the crystallite size and is always higher

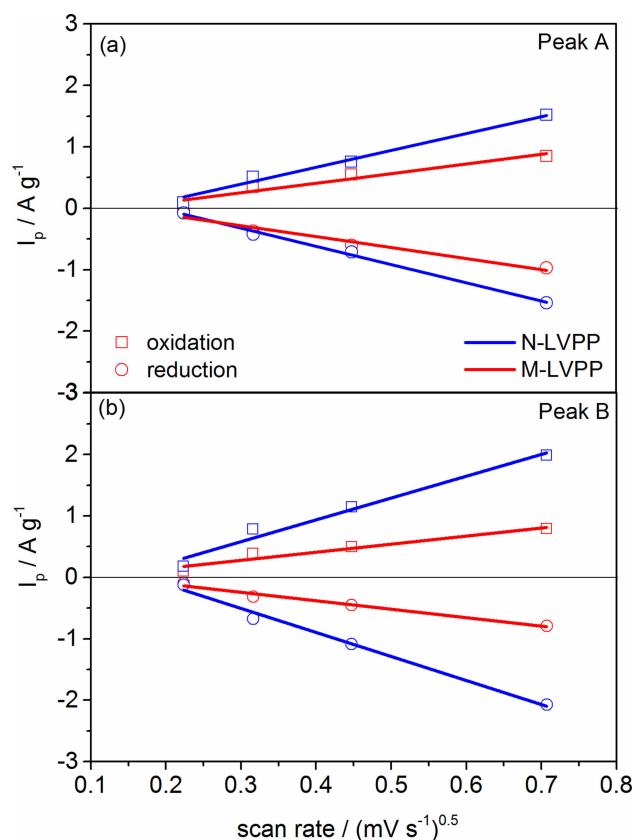


Figure 4. Plot of peak current density versus scan rate of a) peak A at potentials below 4 V and b) peak B at potentials above 4 V for N-LVPP (blue) and M-LVPP (red) electrodes.

Table 2. Calculated apparent diffusion coefficient D_{app}^{Li+} during oxidation/reduction of LVPP between 2 and 4.6 V

Sample name	Oxidation [$cm^2 s^{-1}$]		Reduction [$cm^2 s^{-1}$]	
N-LVPP D_{app}^{Li+}	2.94×10^{-9}	1.37×10^{-9}	1.14×10^{-9}	3.82×10^{-9}
M-LVPP D_{app}^{Li+}	2.52×10^{-9}	6.61×10^{-11}	2.20×10^{-9}	1.02×10^{-9}
current peak	A	B	B	A

for N-LVPP than for M-LVPP, suggesting that the process is faster in nano-crystalline sample. The calculated values of the diffusion coefficient are listed in Table 2. The values obtained for sample N-LVPP is an order of magnitude higher than that of M-LVPP sample, indicating easier Li-ion diffusion for nano crystalline LVPP, as mentioned above. The obtained values lie in the range of similar calculations previously reported for various phosphate materials such as LFP and LVP.^[20,21]

It is known that higher amount of Li ions can be extracted from LVPP by increasing the upper cut off potential to 4.8 V. We have recently reported that a further voltage plateau occurs during the first charge at 4.65 V contributing to the overall capacity.^[19] However, this high voltage plateau disappears after the first cycle. To understand its influence on the cycling behavior, nano-sized LVPP was further investigated. Figures 5a and 5b show the galvanostatic charge/discharge curves of selected cycles at 0.1 C for sample N-LVPP for the first 50 cycles in the potential ranges 2–4.6 V and 2–4.8 V, respectively. When

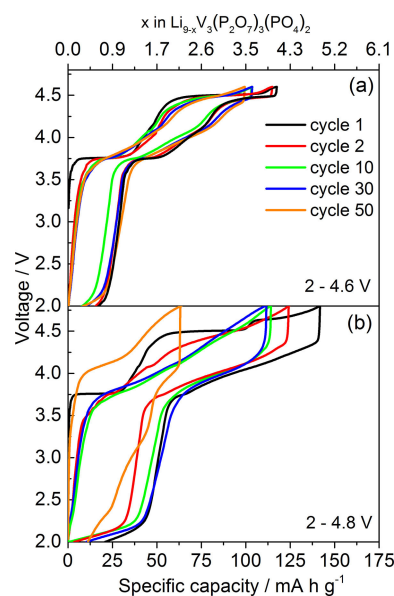


Figure 5. Galvanostatic curves of N-LVPP-based electrodes at 0.1 C in the potential range a) 2.0–4.6 V and b) 2.0–4.8 V.

the upper cut off potential is limited to 4.6 V, a stable specific capacity of 100 mA h g^{-1} with a slight potential drop is obtained. N-LVPP-based electrodes show negligible capacity fading and reversible Li insertion/extraction over 50 cycles. In Figure 5b, almost 5 Li ions per formula unit are extracted during the first charge to 4.8 V, corresponding to a specific capacity of 144 mA h g^{-1} . As expected, in this potential range the third voltage plateau is observed at 4.65 V, and the voltage profile is not retained after the first electrochemical charge. High polarization, significant changes in the voltage profiles and rapid capacity fading are observed upon cycling, in agreement with previously reported results.^[17,19] This electrochemical behavior can be ascribed to different reasons, including irreversible structural changes induced by deep de-lithiation. Unlike LVP, whose electrochemical behavior has been mainly ascribed to the reversible vanadium charge ordering at high potentials, LVPP shows irreversible changes of the electrochemical curves when cycled above 4.6 V.^[12]

Therefore, further investigation of LVPP cathodes from a structural point of view has been performed in order to correlate the mechanism responsible for capacity fading and voltage drop with structural changes occurring at high potentials.

2.3. In Situ and Ex Situ Structural Analysis

In-depth structural characterization of pure Li-monodiphosphate of different transition metal phases has been performed by Poisson et al.^[22] However, to the best of our knowledge, there is only one report available in literature focusing on structural changes of LVPP during de-lithiation/lithiation between 2 and 4.6 V.^[23] The study reported the co-existence of two different phases during de-lithiation without structural

collapse. However, investigations of structural changes and capacity fading mechanism at potentials above 4.6 V have been not reported so far.

In the present study, the structure evolution during cycling was evaluated by applying in situ and ex situ XRD techniques. The in situ XRD investigation was performed on the micro-sized sample M-LVPP within both potential ranges 2–4.6 V and 2–4.8 V, and the results are reported in Figures 6a–d. The

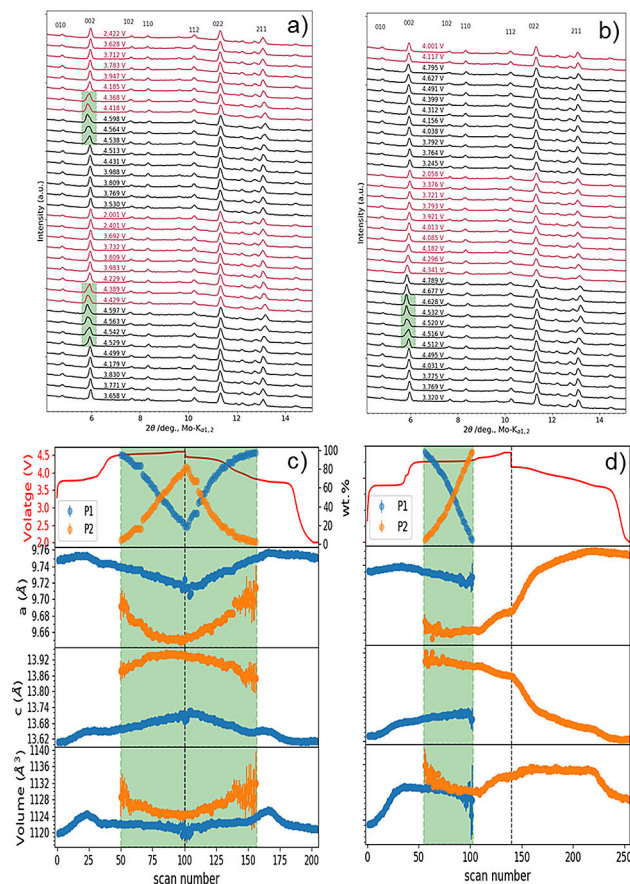


Figure 6. In situ XRD patterns of M-LVPP during galvanostatic cycling (first two cycles) between a) 2 and 4.6 V at 0.027 C and b) 2 and 4.8 V at 0.027 C. Lattice parameter and unit cell volume variation during cycling between c) 2 and 4.6 and d) 2 and 4.8 V (only results for the first cycle are shown).

galvanostatic cycles show that overall 3 Li ions are extracted from M-LVPP within 4.6 V (Figure 6c) and 3.7 Li ions are extracted within 4.8 V (Figure 6d). The lattice parameters obtained for the pristine electrodes before cycling and after cycling at different potentials are summarized in Table 3. The evolution of lattice parameters and unit cell volume up to 4.6 V and 4.8 V are plotted in Figures 6c and 6d, respectively. The values obtained for the pristine electrode are fully consistent with those previously reported for LVPP powders having similar crystallite size.^[19] The first electrochemical de-lithiation step occurs at 3.75 V, which corresponds to the first voltage plateau in the galvanostatic curve. At this potential, the lattice parameters *a* and *c* increase from 9.748 and 13.596 Å to 9.752 and 13.645 Å, respectively, and the trigonal unit cell expands until the extraction of one Li ion per formula unit is complete. Above the 3.75 V voltage plateau, there is a potential slope up to 4.51 V during which the *a* parameter slightly decreases and the *c* parameter slightly increases. During this transition, additional 0.3 Li ions are extracted from the structure according to the galvanostatic curves. Below the potential plateau at 4.51 V, the partially de-lithiated phase, named P1, with an average composition $\text{Li}_{9-y}\text{V}_3(\text{P}_2\text{O}_7)_3(\text{PO}_4)_2$ ($y \leq 1$) has the same space group *P*-3c1 of the original LVPP. During the second voltage plateau at 4.51 V, further 1.7 Li ions are extracted, with an increase of the lattice parameter *c* and a decrease of the lattice parameter *a*, as shown in Figure 6c. The in situ X-ray diffraction pattern (Figure 6a) reveal the occurrence of a shoulder on the low angle side of the 002 peak at a voltage of 4.53 V. The intensity of this new peak grows with further charging. This suggests the emergence of a 2-phase coexistence region at the 4.5 V voltage plateau. This new phase, herein after referred as P2, has the same *P*-3c1 space group symmetry but a larger *c*-axis and a smaller *a*-axis than P1. A 2-phase Rietveld refinement model yields a continuous transformation of the P1 into the P2 phase during the 4.5 V plateau. At the end of the charge process the phase transformation to the P2 phase is not complete and approximately 17 wt-% of the partly de-lithiated P1 phase still exist. In the 2-phase coexistence region, the *a* lattice parameters of both phases decrease while their *c*-axis parameters increase. The observed phase separation reaction was theoretically predicted by Ceder et al.^[18] In their computational investigation of the $\text{Li}_x\text{V}_3(\text{P}_2\text{O}_7)_3(\text{PO}_4)_2$ system they claim that the $x=7$ composition is unstable and separates into $x=6$ and $x=7$ phases. During the following

Table 3. Lattice parameters of phase P1 during de-lithiation/lithiation of M-LVPP from ex-situ XRD.

Sample description	<i>x</i> in $\text{Li}_x\text{V}_3(\text{P}_2\text{O}_7)_3(\text{PO}_4)_2$ ^[a]	<i>a</i> [Å]	<i>c</i> [Å]	Volume [Å ³]
pristine	9	9.744(21)	13.635(43)	1121.49(61)
charged to 4.48 V	7	9.740(34)	13.675(42)	1123.57(51)
charged to 4.6 V	4.85	9.781(18)	13.623(33)	1128.75(45)
charged to 4.7 V	4.4	9.811(20)	13.565(45)	1130.71(24)
charged to 4.8 V	4	9.832(47)	13.538(80)	1134.84(28)
discharged to 2 V (from 4.6 V)	9	9.748(23)	13.625(40)	1120.76(05)
discharged to 2 V (from 4.8 V)	9	9.758(32)	13.613(54)	1122.85(66)
discharged to 2 V (from 4.6 V) after 50 cycles	9	9.798(10)	13.613(22)	1131.90(05)
discharged to 2 V (from 4.8 V) after 50 cycles	9	9.842(01)	13.549(15)	1136.62(33)

[a] Calculated from electrochemical curves.

discharge, when Li is re-intercalated, the phase transformation process and the evolution of the lattice parameters are reversed and at 4.15 V the P2 phase is completely re-converted into the P1 LVPP phase. At the end of the discharge to 2 V, the lattice parameters are very close to the values at the beginning of the first charge. The values obtained for the pristine and cycled electrodes are summarized in Table 1 of Supporting Information.

Figure 6d shows the results of the Rietveld analysis for the in situ diffraction data obtained by applying an upper potential cut-off of 4.8 V. The capacity gain obtained by charging above 4.6 V corresponds to the extraction of additional 0.5 Li ions, besides possible side-reactions with the electrolyte at high-potentials that can also affect the galvanostatic profiles. As can be seen in Figure 6b, also in this case a new peak at the low angle side of the 002 reflex of the partly de-lithiated P1 phase is formed when a voltage of 4.54 V is reached, which indicates a phase separation reaction. The lattice parameter evolution of both phases resembles the evolution of the previous measurement up to 4.6 V. The phase transformation from the P1 to the P2 phase continues on the 4.5 V plateau and is complete when the end of this voltage plateau is reached. Then the voltage increases with a sloping behavior up to 4.8 V. In this voltage region the *a* parameter of the P2 phase increases from 9.65 to

9.68 Å while the *c* parameter decreases from 13.93 to 13.89 Å. During the following discharge process there is no evidence of a re-conversion of phase P2 into phase P1. Only a slight symmetric broadening of the 002 peak can be observed in the voltage range from 4.34 to 4.03 V. Further discharging leads to an increase of the lattice parameter *a* while the *c*-axis decreases again. After complete discharge down to 2 V, the unit cell volume and lattice parameters of P2 LVPP are slightly larger than the original values as summarized in Table 1 of Supporting Information. These results suggest that the phase transitions occurring above 4.6 V up to 4.8 V are mainly irreversible.

As the information about structural changes of nano-sized LVPP were limited by in situ measurements, due to the low intensity of the broad Bragg reflections, ex situ XRD analysis was further carried out on N-LVPP-based electrodes at different states of charge. The diffraction patterns recorded within the potential windows 2–4.6 V and 2–4.8 V are shown in Figures 7a and b, respectively.

The XRD measurements were taken on the pristine electrodes and on electrodes charged at 4.48, 4.60, 4.70 and 4.80 V. As already observed for M-LVPP, the charge process is initially accompanied by an increase in the unit cell volume with increase of the lattice parameter *c* and decrease of the lattice parameter *a*, as shown in Table 3. After charging at 4.48 V, the cathode material is still a single phase (P1) with space group *P*-3c1. As expected, the electrochemical extraction of 4 Li ions within 4.6 V and 5 Li ions within 4.8 V was possible. As shown in inset of Figure 7a, the diffraction pattern of N-LVPP charged to 4.6 V displays peak splitting similar to what already observed during in situ analysis of M-LVPP, indicating a phase transformation into a new phase having the same space group than the pristine LVPP. This is accompanied by an increase in the unit cell volume of phase P1, with increase of the lattice parameter *a* and decrease of the lattice parameter *c* as shown in Table 3. This corroborates with the removal of Li ions from the sites which is in between the layers as described by Poisson et al.^[22] The lattice parameters of phase P2 were found to have smaller *a* parameter (9.670 Å) and larger *c* parameter (14.112 Å) with respect to P1.

On subsequent discharge from 4.6 to 2 V, the phase transformation is reversed, with decreasing of the unit cell volume and restoring of the lattice parameters *a* and *c* to their initial value. The total volume change of phase P1 from the pristine LVPP structure to the partially de-lithiated structure up to 4.6 V is +0.7%. Figure 7b shows the XRD patterns obtained when charging to 4.8 V. During charging from 4.6 to 4.8 V, the unit cell volume of the phase P1 further increases with decrease of *c* and increase of the *a* lattice parameter, as indicated in Table 3. In addition, the calculated lattice parameters of phase P2 are found to be slightly decreased, with *a* = 9.660 and *c* = 14.082 Å. The total volume increase of phase P1 during charge to 4.8 V is 1.25% which is close to the value predicted by DFT calculations.^[18] During subsequent lithiation to 2 V, a broadening of the (0 0 2) Bragg peak occurs with slight change in the intensity of the peaks and increased unit cell volume than that of the pristine LVPP before cycling. In good agreement with in situ XRD results, the ex situ XRD investigation on nano-sized

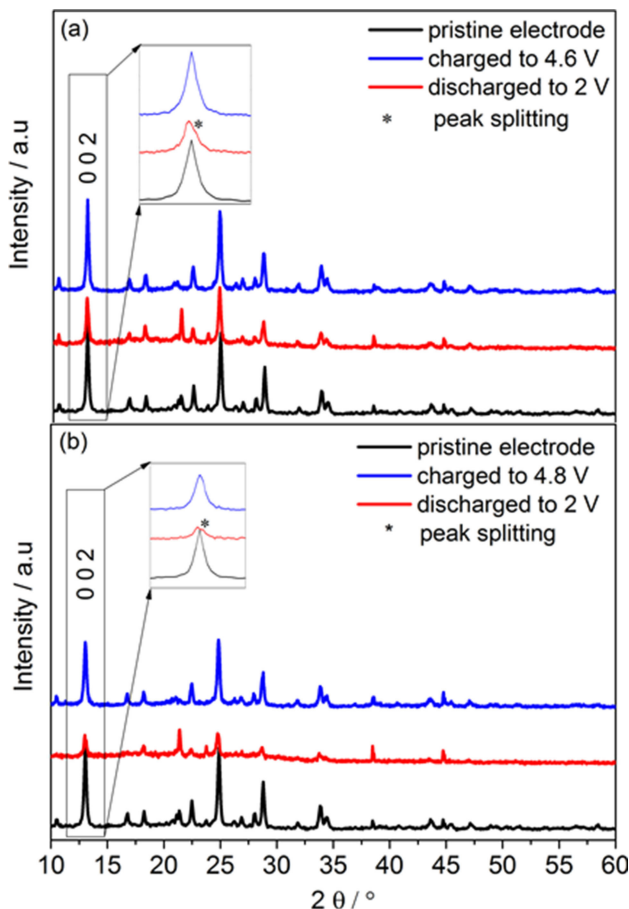


Figure 7. Diffraction patterns of N-LVPP-based electrodes before (pristine) and after one cycle between a) 2 and 4.6 V and b) 2 and 4.8 V.

LVPP electrodes reveals that: 1) during the first electrochemical Li extraction in the potential window 2–4.6 V phase transition occurs with limited changes in the crystal structure, 2) during discharge, the original phase is restored when limiting the upper cut-off to 4.6 V whilst irreversible phase transformations are detected when charging up to 4.8 V, 3) during deep delithiation at potentials higher than 4.6 V, strong changes of lattice parameter c are observed. Therefore when cycling in the wider potential window of 2 and 4.8 V, irreversible phase transformation occurs. In addition, the decreasing of the lattice parameter c during deep de-lithiation at potentials higher than 4.6 V, indicates that some changes in the interlayer distance occurs, which can possibly cause structure collapse.

To further study the structural modifications upon cycling, electrodes made of N-LVPP were analyzed by ex situ XRD after 50 cycles within both potential windows. The obtained diffraction patterns are reported Figure 8a. The patterns of the

prolonged cycling between 2 and 4.6 V leads to a slight increase of the unit cell volume.

After cycling in the potential window 2–4.8 V, instead, the XRD analysis reveals broadening and loss of intensity of the peaks, and a much larger unit cell when compared to the pristine state. This further confirms that the irreversible phase transformations and the reducing of the interlayer distance taking place at high potentials induce strong crystallographic changes affecting the long-term cyclability, capacity retention and columbic efficiency. Similar behavior which was responsible for voltage and capacity fading has been reported for NMC-based layered materials.^[24–25] Additional analysis of these electrodes was carried out by FTIR and the results are shown in Figure 8b. The absorbance spectra of the fresh N-LVPP-based electrodes shows clearly the bands corresponding to the P–O–P bridges between 750 and 900 cm^{-1} , PO_3 bonds at 595, 1055 and 1133 cm^{-1} , PO_4 bonds at 426, 555, 1105 and 1162 cm^{-1} , in good agreement with literature reported data.^[26] When comparing the spectra of the electrode cycled in the potential window 2–4.6 V with the pristine electrode, we observe that the peaks corresponding to the phosphate groups are retained but less intense after cycling. Although the presence of electrolyte degradation products at the surface of the electrodes could affect the FTIR spectra, and possibly reduce the strength of absorbance bands, no additional bands assigned to by-products is observed in the spectra after cycling. The spectrum of the electrode cycled between 2 and 4.8 V shows no clear peaks corresponding to phosphate groups with evident broadening/merging of the absorbance bands. This feature indicates loss of crystallinity due to the structural changes induced by cycling, in good agreement with XRD results.^[27]

Nevertheless, side-reactions between the electrolyte and carbon and/or with the nano-crystalline cathode materials cannot be excluded, especially at such high operating potentials. Goodenough et al. have reported about the spontaneous formation of a surface layer on the interface between electrode and electrolyte for LVP.^[28] In order to clarify the impact of such surface reactions on N-LVPP based electrodes, EIS measurements were carried out. Figure 9 shows the Nyquist plots obtained at different states of charge.

The spectra were initially acquired before the voltage plateau (black lines), where no electrochemical reactions are expected to occur. Afterwards, EIS spectra were recorded at the end of discharge (2 V) on electrodes previously charged to 4.6 (Figure 9a) or 4.8 V (Figure 9b). All of the obtained dispersions show two partially overlapped semicircles: the first one in the high-frequency region, between 100 and 15 kHz, can be related to the formation of a surface film mainly due to the decomposition of the electrolyte components on the electrode surface; the second one in the high to mid-frequency region, between 15 kHz and 15 Hz, is ascribed to the charge-transfer resistance. These two main features of the Nyquist plots are more visible in the inset of Figure 9b. In the low-frequency region, a Warburg line associated with the solid-state diffusion of Li ions is observed. The spectra were fitted based on the equivalent circuit given in Figure 9a.^[29] The resistance associated with the surface film, R_{film} is approximately 0.7 $\Omega \text{ mg}^{-1}$ for

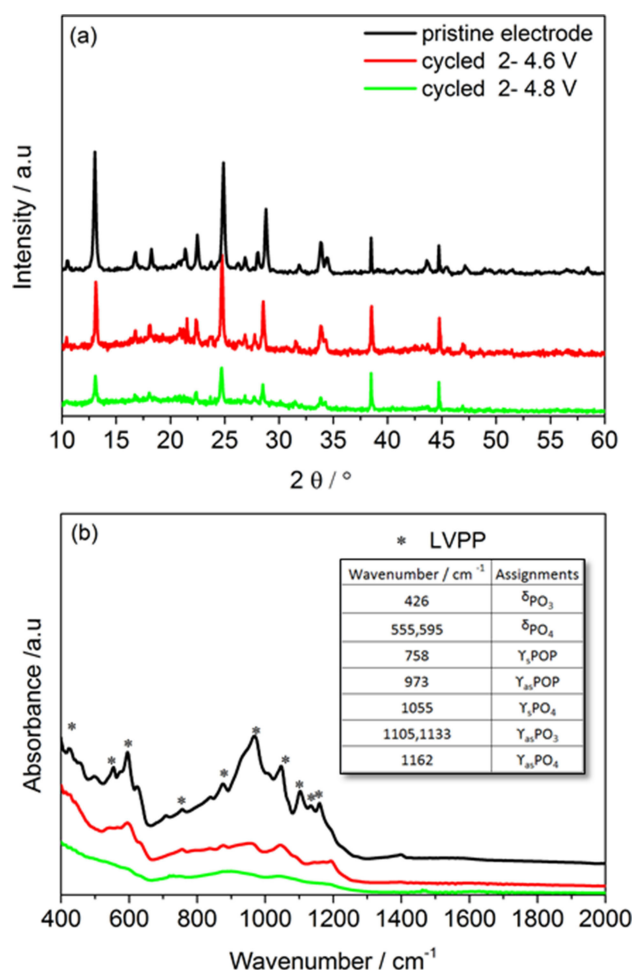


Figure 8. a) XRD patterns and b) FTIR spectra of pristine and cycled N-LVPP-based electrodes. The cycled electrodes have been discharged to 2 V before analysis.

pristine electrode are also reported for sake of comparison. The Rietveld analysis results, reported in Table 3, show that

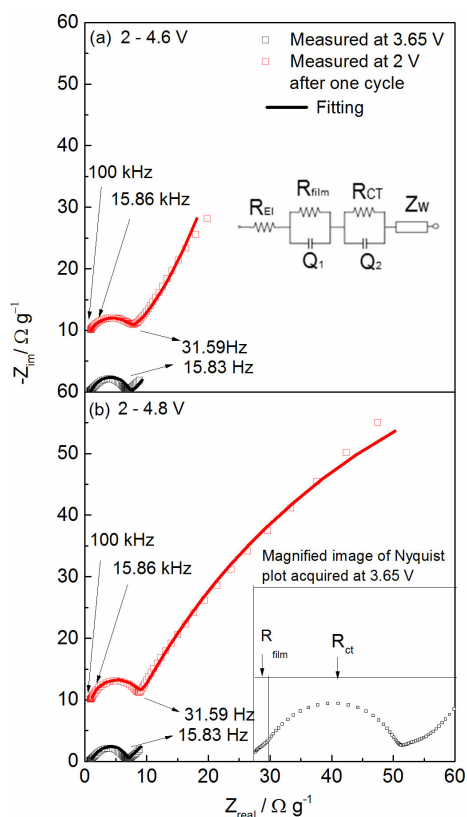


Figure 9. Nyquist plots recorded before charging at 3.65 V (black) and at 2 V after discharging (red) for N-LVPP-based electrodes cycled between a) 2 and 4.6 V and b) 2 and 4.8 V. The fitting is represented by the solid line in all the spectra.

all fresh and cycled electrodes independently from the applied upper cut-off. On the other hand, the resistance associated with the charge-transfer, R_{ct} , slightly increases after one cycle and the increase depends on the applied upper cut-off. Indeed, R_{ct} increases from 5.5 to 6.9 $\Omega \text{ mg}^{-1}$ after cycling between 2 and 4.6 V and from 5.5 to 8.5 $\Omega \text{ mg}^{-1}$ after cycling between 2 and 4.8 V. This indicates that the conductivity of LVPP changes during cycling and that extraction of high amounts of Li, i.e. charging up to 4.8 V, leads to an increase of the resistance associated with the charge-transfer process.

On the basis of these results, we suggest that the side reactions at the electrode/electrolyte interface do not significantly affect the overall electrochemical behavior during the first cycle. The charge-transfer process is instead affected by the amount of Li extracted and that the electronic and ionic properties of the structure are not retained after cycling at high potentials. This may be likely due to the structural changes above described. Therefore, the changes of the electrochemical curves after charging at 4.8 V can mainly be ascribed to the structural modifications rather than to the formation of a surface film. Applying a charge cut-off of 4.6 V limits the specific capacity but also allows minimizing the changes on the structure and on the material properties.

3. Conclusions

Decreasing the crystallite size of LVPP from 190 to 40 nm significantly improves the electrode kinetics. Independent from crystallite size, changes in the voltage profile are observed during charging up to 4.8 V. In situ and ex situ XRD analysis reveals that structural changes occur at potentials above 4.6 V. Unlike other cathode materials, the overall lattice volume of LVPP expands upon electrochemical de-lithiation and no phase transitions are detected below 4.54 V. The unit cell volume linearly increases during de-lithiation and decreases during lithiation. We observed a phase transition at 4.54 V which becomes irreversible after charging up to 4.8 V. The new phase was modelled assuming a second phase of LVPP having the same space group and a larger unit cell. Although the increase of the overall unit cell volume of the original phase after extraction of approximately 5 Li ions is limited to 1.25%, the interlayer distance associated with the lattice parameter c decreases significantly. These findings suggest that the LVPP lattice undergoes irreversible changes and possible structural collapse during deep de-lithiation at potentials above 4.6 V. XRD and FTIR analyses on cycled electrodes indicate that LVPP undergoes progressive loss of crystallinity when cycled between 2 and 4.8 V. Other possible phenomena, such as surface film formation at high potentials, have a limited impact on the observed electrochemical behavior during the first cycle, as suggested by EIS results. The capacity fading upon cycling at potentials above 4.6 V of LVPP-based cathodes is mainly ascribed to the irreversible changes of the pristine layered structure, whose properties as Li-host are affected by the shrinking interlayer distance.

Experimental Section

Synthesis of LVPP

The synthesis of LVPP was performed by the solid-state procedure reported previously.^[19] In order to obtain micro-crystalline LVPP (M-LVPP), the as synthesized LVPP was further treated by preparing dispersion in lactose monohydrate ($\text{C}_{12}\text{H}_{22}\text{O}_{11} \cdot \text{H}_2\text{O}$, Merck) solution. The product was then dried at 80 °C, ground and calcinated at 700 °C for 2 h. For obtaining nano-crystalline LVPP (N-LVPP), the pristine sample was additionally ball milled at 400 rpm for 12 h before being dispersed in the lactose solution. The final carbon content for both the samples as a result of lactose decomposition was determined by Elemental Analysis using EA-4000 instrument from Analytikjena.

Structural Characterization

Ex situ X-ray diffraction patterns were collected on a Siemens BRUKER D5000 by using Cu $K\alpha$ radiation ($\lambda = 0.154 \text{ nm}$) and $\theta/2\theta$ Bragg-Brentano geometry. Cell parameters and average crystallite sizes were calculated from the diffraction data using full-pattern refinement with the Topas (Bruker AXS) software. Ex situ XRD

investigations on electrodes were carried out using air-tight sample holder and all of the samples were washed prior with DMC inside an Ar-filled glove-box with water and oxygen levels below 0.1 ppm to avoid contamination from the atmosphere. All the refinements converged with a fit of $R_p < 12\%$ and $R_{wp} < 17\%$. The in situ X-ray powder diffraction patterns were collected on a dedicated parallel beam laboratory diffractometer in transmission geometry with a microfocus rotating anode, Mo $K_{\alpha 1,2}$ radiation and a Pilatus 300K-W detector. The detector was mounted perpendicular to the incoming beam with a sample-to-detector distance of 320 mm. Details of the diffraction setup can be found in the reference.^[30] The experimental geometry was determined with an annealed CeO_2 powder sample and the pyFAI software package was used for the detector calibration and azimuthal integration of the 2D diffraction images.^[31] The X-ray beam size was adjusted to approximately 2.6 times 1 mm^2 with the aid of a JJ-X-ray slit system. The exposure time for each in situ 2D diffraction image was 300 s. Two consecutive images were added to eliminate cosmic spikes on the detector and to increase the counting statistics resulting in a time resolution of 10 min. The instrumental resolution function of the diffraction setup was determined with the annealed CeO_2 sample and was described with a pseudo-Voigt profile function of Thomson, Cox and Hastings.^[32] To account for possible sample-displacement errors a zero-point correction defined by Norby was used.^[33] In the Rietveld analysis performed with the aid of the TOPAS V5 software the background, lattice parameters, weight fractions and microstructural parameters were refined. The in situ battery cells were coin cell type electrochemical half cells which consist of a LVPP-based cathode, a metallic Li-anode, a Whatman GF/A glass micro fiber separator, a solution of LiPF_6 (1 M) in ethylene carbonate (EC) and dimethyl carbonate (DMC) w/w as electrolyte. The coin cells were cycled under galvanostatic conditions with a C-rate of 0.027 C. Scanning Electron Microscopy (SEM) micrographs and Energy Dispersive X-ray (EDX) analysis were acquired on a Leo-Gemini 1530VP instrument. FTIR measurements were carried out on a Bruker Vertex 70 using a Platinum ATR (Bruker) inside an Ar-filled glove-box (H_2O and O_2 content $< 0.1 \text{ ppm}$). All spectra were obtained at a resolution of 4 cm^{-1} within the range $400\text{--}3000 \text{ cm}^{-1}$.

HR-TEM images were collected using an image-Cs-corrected instrument FEI Titan 80–300 kV allowing atomic resolution at low accelerating voltage of 80 kV as well, where less knock-on damage was expected. The LVPP samples were prepared by crashing using liquid nitrogen and imaged at 80 kV and 300 kV. During beam exposure, the structure undergoes fast amorphization which makes orientation and alignment of the sample much more difficult as usual especially due to the short applicable total exposure time. So, the particular sample preparation process and different TEM accelerating voltages were adopted to minimize the sample damage during electron exposure.

Electrochemical Measurements

The electrodes for electrochemical measurements and in situ XRD analysis were prepared by mixing LVPP (M-LVPP or N-LVPP) as active material with carbon SuperP (Timcal) and PVDF (Solvay) in the ratio 80:10:10 wt%. The slurry was coated onto an Al foil with doctor blade technique (coating thickness of $150 \mu\text{m}$) and dried at 70°C overnight. Electrodes of 12 mm diameter were cut and pressed to improve contact between active and non-active materials and current collector. The active material loading of all the electrodes was approximately 3.5 mg cm^{-2} . After being dried at 105°C under vacuum overnight, the electrodes were transferred to an Ar-filled glove-box with H_2O and O_2 content below 0.1 ppm. Electrodes with higher loading of 11 mg cm^{-2} were prepared for

in situ XRD analysis. The electrochemical measurements were performed in T-cells where metallic Li was used as reference and counter electrode, GF/A as a separator and battery-grade LiPF_6 1 M solution in EC: DMC 1:1 w/w (UBE Industries) as electrolyte. The current rates were calculated assuming $1 \text{ C} = 173.45 \text{ mAh g}^{-1}$. All measurements were carried out using a VMP2/Z electrochemical workstation (Bio-logic Science Instruments). EIS measurements were carried out by using ECC-Ref electrochemical cells (EL-Cell GmbH) with metallic Li as reference electrode. The measurements were carried out in a climate controlled chamber where the temperature was maintained at $T = 20^\circ\text{C}$ and the spectra were acquired in the frequency range 10 mHz to 100 kHz at different states of charge. The electrodes were galvanostatically cycled at 0.1 C. A potentiostatic step of 1 h was given to the electrodes as an equilibrium time before obtaining the spectra where the potential change at the end of the equilibrium time was 0.4 mV. The spectra were fit using Z-fit program in EC-lab software. All the fit converged with an error value of 0.007. All potentials are referred to Li^+/Li . All tests were performed two or more times and the obtained results showed very good reproducibility.

Acknowledgements

This work was supported by the German Federal Ministry of Education and Research (BMBF) in the project Li-EcoSafe (03X4636 A). The author would like to thank Gisela Arnold (ZSW) for Elemental Analysis and Claudia Pfeifer (ZSW) for SEM/EDX analysis and fruitful discussions on XRD results.

Conflict of Interest

The authors declare no conflict of interest.

Keywords: Li-ion batteries • energy conversion • Structure elucidation • electrochemistry • X-ray diffraction

- [1] K. Zaghib, A. Guerfi, P. Hovington, A. Vijn, M. Trudeau, A. Mauger, J. B. Goodenough, C. M. Julien, *J. Power Sources* **2013**, 232, 357–369.
- [2] C. Masquelier, L. Croguennec, *Chem. Rev.* **2013**, 113, 6552–6591.
- [3] G. Hautier, A. Jain, T. Mueller, C. Moore, S. P. Ong, G. Ceder, *Chem. Mater.* **2013**, 25, 2064–2074.
- [4] A. Padhi, K. Nanjundaswamy, J. B. Goodenough, *J. Electrochem. Soc.* **1997**, 144, 1188–1194.
- [5] N. N. Bramnik, K. G. Bramnik, T. H. Buhrmester, C. Baehtz, H. Ehrenberg, H. Fuess, *J. Solid State Electrochem.* **2004**, 8, 558–564.
- [6] R. Ruffo, R. A. Huggins, C. M. Mari, M. Piana, W. Weppner, *Ionics* **2005**, 11, 213–219.
- [7] J. Vetter, P. Novak, M. R. Wagner, C. Veit, K.-C. Moller, J. O. Besenhard, M. Winter, M. Wohlfahrt-Mehrens, C. Vogler, A. Hammouch, *J. Power Sources* **2005**, 147, 269–281.
- [8] M. Gauthier, T. J. Carney, A. Grimaud, L. Giordano, N. Pour, H.-H. Chang, D. P. Fenning, S. F. Lux, O. Paschos, C. Bauer, F. Maglia, S. Lupart, P. Lamp, Y. S-Horn, *J. Phys. Chem. Lett.* **2015**, 6, 4653–4672.
- [9] R. Hausbrand, G. Cherkashinin, H. Ehrenberg, M. Gröting, K. Albe, C. Hess, W. Jaegermann, *Mater. Sci. Eng. B.* **2015**, 192, 3–25.
- [10] M. Mancini, E. Bekaert, T. Diemant, M. Marinaro, L. de Biasi, R. J. Behm, M. Wohlfahrt-Mehrens *Electrochimica Acta.* **2015**, 176, 679–688.
- [11] G. Gabrielli, P. Axmann, M. Wohlfahrt-Mehrens, *J. Electrochem. Soc.* **2016**, 163, A470–A476.
- [12] S. C. Yin, H. Grondy, P. Strobel, M. Anne, L. F. Nazar, *J. Am. Chem. Soc.* **2003**, 125, 10402–10411.

- [13] J. Barker, R. K. B. Gover, P. Burns, A. Bryan, *Electrochem and Solid-State Letters*. **2005**, *8*, A446–A448.
- [14] K. L. Harrison, C. A. Bridges, C. U. Segre, C. D. Varnado Jr., D. Applestone, C. W. Bielawski, M. P. Paranthaman, A. Manthiram *Chem. Mater.* **2014**, *26*, 3849–3861.
- [15] S. Kim, Z. Zhang, S. Wang, L. Yang, E. J. Cairns, J. E. Penner-Hahn, A. Deb, *J. Phys. Chem. C*. **2016**, *120*, 7005–7012.
- [16] L. Wang, J. Xu, C. H. Wang, X. Cui, J. Li, Y.-N. Zhou, *RSC Adv.* **2015**, *5*, 71684–71691.
- [17] Q. Kuang, J. Xu, Y. Zhao, X. Chen, L. Chen, *Electrochim. Acta*. **2011**, *56*, 2201–2205.
- [18] A. Jain, G. Hautier, C. Moore, B. Kang, J. Lee, H. Chen, N. Twu, G. Ceder, *J. Electrochem. Soc.* **2012**, *159*, A622–A633.
- [19] P. Balasubramanian, M. Mancini, P. Axmann, M. Wohlfahrt-Mehrens, *J. Electrochem. Soc.* **2017**, *164*, A6047–A6053.
- [20] A. V. Ivanishchev, A. V. Churikov, I. A. Ivanishcheva, *Ionics*. **2016**, *22*, 483–501.
- [21] H. Liu, G. Yang, X. Zhang, P. Gao, L. Wang, J. Fang, J. Pinto, X. Jiang, *J. Mater. Chem.* **2012**, *22*, 11039–11047.
- [22] S. Poisson, F. d'Yvoire, N. G. H. Dung, E. Bretey, P. Berthet, *J. Solid State Chem.* **1998**, *138*, 32–40.
- [23] Q. Kuang, Z. Lin, Y. Zhao, X. Chen, L. Chen, *J. Mater. Chem.* **2011**, *21*, 14760–14765.
- [24] J. Yang, Y. Xia, *ACS Appl. Mater. Interfaces*. **2016**, *8*, 1297–1308.
- [25] J.-L. Shi, J.-N. Zhang, M. He, X.-D. Zhang, Y.-X. Yin, H. Li, Y.-G. Guo, L. Gu, L.-J. Wan, *ACS Appl. Mater. Interfaces* **2016**, *8*, 20138–20146.
- [26] F. Capitelli, N. Dridi, E. H. Arbib, V. Valentini, G. Matteil, *Z. Kristallogr.* **2007**, *222*, 521–526.
- [27] A. A. Salah, P. Jozwiak, K. Zaghib, J. Garbarczyk, F. Gendron, A. Mauger, C. M. Julien, *Spectrochim. Acta A Mol. Biomol. Spectrosc.* **2006**, *65*, 1007–1013.
- [28] N. Membreno, K. Park, J. B. Goodenough, K. J. Stevenson, *Chem. Mater.* **2015**, *27*, 3332–3340.
- [29] D. Aurbach, M. D. Levi, E. Levi, H. Teller, B. Markovsky, G. Salitra, *J. Electrochem. Soc.* **1998**, *145*, 3024–3034.
- [30] L. De Biasi, G. Lieser, J. Rana, S. Indris, C. Dräger, S. Glatthaar, R. Mönig, H. Ehrenberg, J. R. Binder, H. Geßwein, *CrystEngComm*. **2015**, *17*, 6163–6174.
- [31] J. Kieffer, G. Ashiotis, A. Deschildre, Z. Nawaz, J. P. Wright, D. Karkoulis, F. E. Picca *J. Appl. Cryst.* **2015**, *48*, 510–519.
- [32] P. Thompson, D. E. Cox, J. B. Hastings, *J. Appl. Cryst.* **1987**, *20*, 79–83.
- [33] P. Norby, *J. Appl. Cryst.* **1997**, *30*, 21–30.

Manuscript received: July 18, 2017
Version of record online: November 3, 2017